REPORT DOCUMENTATION PAGE

AFRL-SR-BL-TR-02-
0143

1. REPORT DATE (DD-MM-YYYY) 07-03-2002	2. REPORT TYPE Final		..., 02/1998-30/06/2001

4. TITLE AND SUBTITLE	5a. CONTRACT NUMBER
A Novel Compuational Approach to Combustion Modelling	
	5b. GRANT NUMBER F49620-98-1-0206
	5c. PROGRAM ELEMENT NUMBER

6. AUTHOR(S)	5d. PROJECT NUMBER
Paolucci, Samuel	
	5e. TASK NUMBER
Powers, Joseph M.	
	5f. WORK UNIT NUMBER

7. PERFORMING ORGANIZATION NAME(S) AND ADDRESS(ES)	8. PERFORMING ORGANIZATION REPORT
Department of Aerospace and Mechanical Engineering University of Notre Dame Notre Dame, IN 46556-5637	**20020419 174**

9. SPONSORING / MONITORING AGENCY NAME(S) AND ADDRESS(ES)	10. SPONSOR/MONITOR'S ACRONYM(S)
AFOSR 801 N. Randolph St. Room 732 Arlington, VA 22203-1977	AFOSR
	11. SPONSOR/MONITOR'S REPORT NUMBER(S)

12. DISTRIBUTION / AVAILABILITY STATEMENT

13. SUPPLEMENTARY NOTES

14. ABSTRACT
A novel wavelet adaptive multilevel representation (WAMR) algorithm combined with an extended intrinsic low dimensional manifold (ILDM) approach to solve challenging multiscale problems has been developed. The emphasis of this work was the development of a combined algorithm to rationally reduce to lower dimensions the differential equations that model unsteady, multi-dimensional combustion processes. In particular, there was a focus on problems in which there is full coupling between fluid mechanics and chemical kinetics. Such problems are characterized by a multiplicity of phenomena evolving over length and time scales which are widely disparate. Results are shown for a resolved viscous one-dimensional detonation in hydrogen/oxygen/argon with detailed kinetics. The method has been extended to multiple dimensions, and results are shown for flow in a lid-driven cavity at high Reynolds number.

15. SUBJECT TERMS
Combustion, Numerical Methods, Wavelets, Reduced Chemistry

16. SECURITY CLASSIFICATION OF:			17. LIMITATION OF ABSTRACT	18. NUMBER	19a. NAME OF RESPONSIBLE PERSON Maj. W. M. Hilbun
a. REPORT U	b. ABSTRACT U	c. THIS PAGE U	UU	25	19b. TELEPHONE NUMBER (include area code) 703-696-8429

Standard Form 298 (Rev. 8-98)
Prescribed by ANSI Std. Z39.18

Executive Summary

The scope of this project has been the development of a combined algorithm based on a wavelet adaptive multilevel representation (WAMR) method and a technique to rationally reduce to lower dimensions the differential equations that model unsteady, multi-dimensional combustion processes, known as the intrinsic low-dimensional manifold, or ILDM.

We focus on problems in which there is full coupling between fluid mechanics and chemical kinetics. Such problems are characterized by a multiplicity of phenomena evolving over length and time scales which are widely disparate. In brief, the wavelet decomposition adaptively reduces the total number of unknowns in space, and the rational reduction, which applies ILDM theory, subsequently reduces the dimension of the local manifold on which the chemical reactions evolve. The first step of the method utilizes a multilevel wavelet collocation approximation. The multilevel structure of the algorithm facilitates the computational adaptation of the grid refinement according to the temporal evolution of the solution. One of the strengths of the adaptive wavelet collocation technique is its ability to allow high resolution computations only in regions where sharp variations occur. Thus, far fewer unknowns are needed for wavelets than for conventional finite-difference or finite-element techniques. Numerical solutions have shown the ability of the wavelet method to resolve localized structures, whose positions and sharpness change both spatially and temporally. In the ILDM phase of the computation, a local linear analysis gives the time scales associated with the reactions. Those processes which occur on time scales faster than a physically motivated cutoff time scale are allowed to relax to partial equilibrium; the remaining processes are subjected to time evolution. Consequently, the number of differential equations to be solved is reduced, and those that remain are significantly less stiff. This reduction results in a more efficient numerical method.

We demonstrate the numerical algorithm by considering a standard ignition delay problem for a mixture of hydrogen/oxygen/argon in a shock tube. An operator splitting method is used to describe the reactions as a system of ordinary differential equations at each spatial point. The ILDM method is used to eliminate the stiffness associated with the chemistry by decoupling processes which evolve on fast and slow time scales. The fast time scale processes are systematically equilibrated, thereby reducing the dimension of the phase space required to describe the reactive system. The WAMR technique captures the detailed spatial structures automatically with a small number of basis functions thereby further reducing the number of variables required to describe the system. A maximum of only 300 collocation points and 15 scale levels yields results with striking resolution of fine scale viscous and induction zones. Additionally, the resolution of physical diffusion processes minimizes the effects of potentially reaction-inducing artificial entropy layers associated with numerical diffusion.

To demonstrate the multidimensional capability of the WAMR algorithm, we present results for a classical benchmark problem: the two-dimensional lid driven cavity. The problem is studied at sufficiently large Reynolds numbers so that solutions using conventional numerical methods become difficult to obtain due to the increasing presence of multiscale structures.

The work is not incremental in character and in fact represents a substantially new approach which we believe has yielded consequent dividends. While additional generalizations can and should be made to the algorithm, we nevertheless believe the research has set a new standard in high performance computing applied to combustion. In addition we believe the combined novelty and utility of the WAMR/ILDM method will have ramifications extending into the other areas of computational physics.

The following personnel were involved in the project:

- Samuel Paolucci, Professor,

- Joseph M. Powers, Associate Professor,

- Christopher Bowman, Post-Doctoral Research Associate,

- Sandeep Singh, Graduate Research Assistant,

- Yevgenii Rastigejev, Graduate Research Assistant,

and the following publications resulted from this work:

Powers, J. M., Paolucci, S., Rastigejev, Y., and Singh, S., 1999, "A Wavelet/ILDM Method for Computational Combustion," *Bulletin of the American Physical Society*, Vol. 44, No. 8, p. 54.

Rastigejev, Y., and Paolucci, S., 1999, "The Use of Wavelets in Computational Fluid Mechanics," in *Proceedings of the 3rd ASME/JSME Joint Fluids Engineering Conference*, Paper FEDSM99-7162.

Rastigejev, Y., Singh, S., Bowman, C., Paolucci, S., and Powers, J. M., 2000, "Novel Modeling of Hydrogen/Oxygen Detonation," AIAA-2000-0318, 38th AIAA Aerospace Sciences Meeting and Exhibit, Reno, NV.

Rastigejev, Y., and Paolucci, S., 2002, "Wavelet Based Adaptive Multilevel Algorithm for Solving PDEs," *Journal of Scientific Computing*, to be submitted.

Singh, S., Powers, J. M., and Paolucci, S., 1999, "Multidimensional Detonation Solutions from Reactive Navier-Stokes Equations," Proceedings of the 17th International Colloquium on the Dynamics of Explosions and Reactive Systems, Heidelberg, Germany.

Singh, S., and Powers, J. M., 1999, "Modeling Gas Phase RDX Combustion with Intrinsic Low Dimensional Manifolds," Proceedings of the 17th International Colloquium on the Dynamics of Explosions and Reactive Systems, Heidelberg, Germany.

Singh, S., Rastigejev, Y., Paolucci, S., and Powers, J. M., 2001, "Resolved Viscous Detonation in $H_2/O_2/Ar$ Using Intrinsic Low Dimensional Manifolds and Wavelet Adaptive Multilevel Representation," *Combustion Theory and Modeling*, Vol. 5, pp. 163-184.

Vasilyev, O. V., and Bowman, C., 2000, "Second-Generation Wavelet Collocation Method for the Solution of Partial Differential Equations," *Journal of Computational Physics*, Vol. 165, pp. 660-693.

1 Introduction

Here we discuss a novel wavelet adaptive multilevel representation (WAMR) algorithm combined with an extended intrinsic low dimensional manifold (ILDM) approach to solve challenging multiscale problems. The emphasis of this work is the development of a combined algorithm to rationally reduce to lower dimensions the differential equations that model unsteady, multi-dimensional combustion processes In particular, there is a focus on problems in which there is full coupling between fluid mechanics and chemical kinetics. Such problems are characterized by a multiplicity of phenomena evolving over length and time scales which are widely disparate. In brief, the WAMR algorithm adaptively reduces the total number of unknowns in space, and the rational reduction, which applies ILDM theory, subsequently reduces the dimension of the local manifold on which the chemical reactions evolve. The multilevel structure of the algorithm facilitates the computational adaptation of the grid refinement according to the temporal evolution of the solution. One of the strengths of the adaptive wavelet collocation technique is its ability to allow high resolution computations only in regions where sharp variations occur. Thus, far fewer unknowns are needed for wavelets than for conventional finite-difference or finite-element techniques. Numerical solutions have shown the ability of the wavelet method to resolve localized structures, whose positions and sharpness change both spatially and temporally. In the ILDM phase of the computation, a local linear analysis gives the time scales associated with the reactions. Those processes which occur on time scales faster than a physically motivated cutoff time scale are allowed to relax to partial equilibrium; the remaining processes are subjected to time evolution. Consequently, the number of differential equations to be solved is reduced, and those that remain are significantly less stiff. This reduction results in a more efficient numerical method. To demonstrate the algorithm's capabilities, we present results for a shock tube ignition delay problem and a two-dimensional high Reynolds number lid-driven cavity problem. We give below a brief discussion of some of the challenges that exist in simulating realistic combustion problems for which our algorithm is well suited.

A typical combustion event in devices of practical importance can be described as a highly coupled process involving a large number of elementary chemical reactions evolving simultaneously within a complex flow field. It is clear in many applications that chemical kinetics affects the motion of the fluid, and moreover, the motion of the fluid affects the chemical kinetics. One of the key problems in theoretical combustion science is to generate reliable solutions to equations which model these systems. Often these models consist of equations representing hundreds of elementary reaction steps coupled with full compressible Navier-Stokes equations. Successful modeling has the potential to yield more precise design and control strategies for a wide variety of practical devices such as propulsion systems, internal combustion engines, incinerators, or furnaces.

In the past decade, improved computer hardware has made practical the numerical modeling of processes with both detailed chemical kinetics and fluid mechanics. Examples, such as laminar diffusion flames, are discussed by, among many others, Smooke, 1991a. The kinetic schemes involved are typically quite large, involving hundreds of reactions and dozens of chemical species, *cf.* Warnatz, 1992. As discussed by Maas and Pope (MP), 1992b, typical reaction kinetic schemes can involve processes which evolve over widely disparate time scales, ranging typically from 10^{-9} s to 10^2 s. These time scales often eclipse those scales typically associated with fluid mechanical phenomena which are governed often by advection, diffusion, and turbulence. Consequently, fluid mechanics problems, which are often complicated by simultaneous phenomena occurring on micro- and macro-scales, are made even more daunting by the addition of chemical reactions which occur on both faster and slower time scales than those of the fluid mechanics. As a fully converged numerical solution to a set of equations requires a full resolution of *all* space and time scales, completely resolved solutions of multi-dimensional unsteady flow fields using full reaction kinetics are essentially impossible with existing computer hardware and will be for some time to come.

These difficulties have motivated a widespread effort in recent years to identify ways to reduce the complexity of kinetic models while simultaneously retaining the flavor of the full kinetic model, cf. Smooke, 1991b; Radhakrishnan, 1991; Frenklach, 1991; Frenklach, Wang, and Rabinowitz, 1992; Treviño and Méndez, 1992; Goussis and Lam, 1992; Buckmaster, 1993; Lam, 1993; Maas and Pope, 1992a, 1994; Eggles and DeGoey, 1995; Schmidt, *et al.*, 1996, or Vlachos, 1996. The emphases in these studies has been on problems which can be modeled as systems of ordinary differential equations, such as closed homogeneous reactors or steady wave propagation. The more challenging problems in which systems evolve in both space and time

have received almost no scrutiny. Such systems are well-suited for solution via a novel wavelet algorithm combined with an extended ILDM approach. We have recently made some inroads to this end: Rastigejev and Paolucci, 1999; Singh, Powers, and Paolucci, 1999; Singh and Powers, 1999; Powers, Paolucci, Rastigejev, and Singh 1999; Rastigejev, Singh, Bowman, Paolucci, and Powers, 2000; Singh, Rastigejev, Paolucci, and Powers, 2001; Rastigejev and Paolucci, 2002. We discuss these methods and the progress made in the following sections.

2   General Problem Description

Here we describe in a highly abbreviated form the set of unsteady, compressible, reactive Navier-Stokes equations in D ($D = 1, 2$, or 3) spatial variables. These equations are a non-linear system of partial differential equations in spatial variables x_i ($i = 1, \ldots, D$) and time t:

$$\frac{\partial}{\partial t}(\rho) + \frac{\partial}{\partial x_i}(\rho u_i) = 0, \tag{1}$$

$$\frac{\partial}{\partial t}(\rho u_i) + \frac{\partial}{\partial x_j}(\rho u_i u_j + p - \tau_{ij}) = 0, \tag{2}$$

$$\frac{\partial}{\partial t}\left(\rho\left(e + \frac{u_i u_i}{2}\right)\right) + \frac{\partial}{\partial x_i}\left(\rho u_i\left(e + \frac{u_j u_j}{2}\right) + u_j(p\delta_{ij} - \tau_{ij}) + J_i^q\right) = 0 \tag{3}$$

$$\frac{\partial}{\partial t}(\rho y_l) + \frac{\partial}{\partial x_i}(\rho u_i y_l + j_l) = 0, \tag{4}$$

$$\frac{\partial}{\partial t}(\rho Y_n) + \frac{\partial}{\partial x_i}(\rho u_i Y_n + J_n^m) = \dot{\omega}_n \mathcal{M}_n. \tag{5}$$

Dependent variables are density ρ; velocity vector u_i; internal energy e; element mass fractions y_l, where $l = 1, \ldots, L - 1$, and there are L elements; species mass fractions Y_n, where $n = 1, \ldots, N - L$, and there are N species, pressure p, viscous stress τ_{ij}, energy flux J_i^q, element flux j_l, diffusive species flux J_n^m, and species production rate $\dot{\omega}_n$. Here $\mathcal{M}_n$ is the species molecular mass, and δ_{ij} is the Kronecker delta. The above equations describe the conservation of mass, linear momenta, energy, and element mass fractions, respectively, along with the time evolution of species mass fractions. The set of equations is completed when constitutive equations for energy, pressure, heat flux, viscous stress, and species production rates are given. Examples of complete formulation of these terms is standard and given, for instance by Buckmaster and Ludford, 1982, or Williams, 1985.

The governing equations can be written in the form

$$\frac{\partial}{\partial t}\mathbf{u}(x_i, t) = -\frac{\partial}{\partial x_i}\mathbf{f}(\mathbf{u}(x_i, t)) + \mathbf{g}(\mathbf{u}(x_i, t)), \qquad \mathbf{u}, \mathbf{f}, \mathbf{g} \in \Re^{N+D+1}, \tag{6}$$

$$\mathbf{u} \equiv \left(\rho, \rho u_i, \rho\left(e + \frac{u_j u_j}{2}\right), \rho y_l, \rho Y_n\right)^T. \tag{7}$$

Here, we have defined $\mathbf{u}$ as a vector of length $N + D + 1$ dependent variables. The vector $\mathbf{f}$, which can be written as a function of $\mathbf{u}$, models the advective and diffusive fluxes of $\mathbf{u}$, and the vector $\mathbf{g}$ represents a source due to chemical reaction.

3   Operator Splitting

Equation (6) is solved in two steps, a reaction step and a convection-diffusion step, using Strang-splitting (Strang, 1968) . This splitting results in second order accuracy in time. The set of partial differential equations is reduced to ordinary differential equations at each spatial node k by a wavelet collocation method to be described shortly. In the first step, we suppress advection and diffusion, and account for reaction. Suppression of advection and diffusion results in homogeneous equations for mass, linear momenta, energy, and element mass fraction which can be integrated analytically so as to leave only $N - L$ equations to integrate. We then suppress reaction and solve the ODEs which account for advection and diffusion using the wavelet method.

4

3.1 Reaction step

In Step 1, the following equation, equivalent to that for a homogeneous premixed reactor at every point in the space, is solved at each spatial point

$$\frac{\partial \mathbf{u}}{\partial t} = \mathbf{g}(\mathbf{u}).$$

(8)

The first $1 + D + L$ equations of Equation (8) are homogeneous and can be integrated exactly to give

$$\rho = \rho_o \qquad u_i = u_{io} \qquad e = e_o \qquad y_l = y_{lo} \quad (l = 1, \ldots, L-1).$$

(9)

Hence, the $N - L$ species evolution equations in Equation (8) reduce to the following partial differential equations, which are treated at each point in space as ordinary differential equations with ρ, u_i, e, and y_l held constant to the values given in Equation (9) every time this step is repeated:

$$\frac{\partial Y_i}{\partial t} = \frac{\dot{\omega}_i M_i}{\rho_o} \qquad (i = 1, \ldots, N-L).$$

(10)

It is noted that during a single time step the values of ρ_o, e_o, u_{io}, and y_{lo} do not change; because of convection and diffusion, in general, all will change with time.

It can be shown that $\dot{\omega}_i$ can be cast in terms of Y_i for $i = 1, \ldots, N-L$; thus, Equations (10) are well posed and can be solved in their entirety by any standard implicit or explicit technique at every point in space. Because the equations are stiff, we can use the LSODE software package, Hindmarsh, 1983, in full implicit mode when solving the full set of Equations (10). Alternatively, Equations (10) can be solved using the ILDM method, described in a following section, which systematically removes the stiffness associated with reactions. When using the ILDM method, we use a simpler explicit Runge-Kutta method for time advancement, which is second order accurate in time. The size of the time step is dictated by the convection-diffusion time step restriction.

3.2 Convection-diffusion step

In Step 2, the following equation, which is a set of partial differential equations, is solved for the convection diffusion step:

$$\frac{\partial \mathbf{u}}{\partial t} = -\frac{\partial}{\partial x_i} \mathbf{f}(\mathbf{u}).$$

(11)

Again, Equation (11) can be solved by a variety of standard discretization techniques developed for inert fluid mechanics. Here we use the WAMR technique, as discussed in detail by Vasilyev and Paolucci, 1996, 1997. The method is summarized as follows. At any given time step, the pressure, temperature, density, and velocity fields are projected onto a multilevel wavelet basis. The amplitudes of the wavelet basis functions give a measure of the importance of a particular wavelet mode. Additionally, one has available *a priori* error estimates, in contrast to most gradient-based adaptive mesh refinement techniques. All wavelets whose amplitude are below a defined threshold are removed. Calculations are performed for each wavelet whose amplitude is above the threshold (essential wavelets) and for a certain number below the threshold (neighboring wavelets). If at the completion of a time step, an essential wavelet has its amplitude drop below the threshold, it is reclassified as a neighboring wavelet or eliminated, and the neighboring region is adjusted; similarly, if a wavelet in the neighboring region has its amplitude become sufficiently large, it is reclassified as an essential wavelet, and the neighboring region is adjusted. The method is based on a collocation strategy using the auto-correlation functions of the Daubechies scaling function and wavelet of order four as bases. A linearized trapezoidal (implicit) scheme in conjunction with GMRES iterations is used for time advancement. The size of the time step is chosen to satisfy a CFL condition associated with the fastest local velocity.

4 Intrinsic Low Dimensional Manifolds

As noted above, each discrete point in space behaves as an adiabatic, homogeneous premixed reactor, thus enabling the use of the ILDM technique. The method provides a systematic way to overcome the severe stiffness which is associated with full models of gas phase combustion, and thus significantly improves computational efficiency. The ILDM method systematically eliminates the stiffness by equilibrating fast time scale events and describing parametrically a low dimensional manifold upon which slow time scale events evolve.

Here, the method of Maas and Pope, 1992b, slightly adapted for our system, is summarized. The constant density, isochoric, adiabatic combustion for the homogeneous premixed system is described by Eq. (10). The remaining L mass fractions are computed from algebraic constraints described in full by Singh, $et\ al.$, 2001. For gases in the mixture, which are thermally perfect, the specific internal energy of each component is at most a function of temperature. Hence, knowledge of the mass fractions and mass-averaged specific internal energy e_o allows one to use Newton's method to invert the caloric state equation to form $T = T(Y_1, \ldots, Y_{N-L}; e_o, y_{1_o}, \ldots, y_{(L-1)_o})$. Hence, $\dot{\omega}_i$, which is in general a function of temperature, density, and species mass fractions, can now be considered as a function of only $N - L$ of the species mass fractions for fixed values of e_o, ρ_o, and y_{lo}:

$$\dot{\omega}_i = \dot{\omega}_i(Y_1, \ldots, Y_{N-L}; e_o, \rho_o, y_{1_o}, \ldots, y_{(L-1)_o}), \qquad i = 1, \ldots, N - L. \tag{12}$$

Both $\dot{\omega}_i$ and e_i can be easily evaluated using the Chemkin III, Kee, $et\ al.$, 1990, package. Equation (10) can thus be rewritten as

$$\frac{d\mathbf{Y}}{dt} = \mathbf{G}(\mathbf{Y}), \tag{13}$$

where $\mathbf{Y} = (Y_1, \ldots, Y_{N-L})^T$ and $\mathbf{G}(\mathbf{Y}) = \left(\frac{\dot{\omega}_1 M_1}{\rho_o}, \ldots, \frac{\dot{\omega}_{N-L} M_{N-L}}{\rho_o}\right)$. The reciprocals of the eigenvalues of the Jacobian $\mathbf{G_Y}$ at any point in the composition space identify the $N - L$ associated characteristic time scales. The corresponding eigenvectors identify the directions in which each eigenmode of the total trajectory evolves in composition space. The ILDM is identified by a set of points in the composition space where the composition space velocity vector $\mathbf{G}$ is orthogonal to the eigenvectors associated with fast time scales.

We outline here the analysis to compute the ILDM given in detail for a similar system first by Maas and Pope, 1992b, and later extended by Maas, 1998, following the general theory given by Golub and Van Loan, 1996. We choose to resolve M slow time scales; this will result in the choice of M species which will form part of the parameterization for the complete ILDM. This is formed via the following steps. First we decompose the Jacobian matrix $\mathbf{G_Y}$ with a real Schur decomposition:

$$\mathbf{G_Y} = \mathbf{Q} \cdot \mathbf{U} \cdot \mathbf{Q}^T, \tag{14}$$

where $\mathbf{Q}$ is the $(N - L) \times (N - L)$ orthogonal matrix of real Schur vectors and $\mathbf{U}$ is an $(N - L) \times (N - L)$ upper-triangular matrix with eigenvalues along the main diagonal. Typically most eigenvalues are negative and real; for closed adiabatic systems near equilibrium, there is a guarantee of real negative eigenvalues. The matrix is ordered so that proceeding down the diagonal, the real part of the eigenvalue becomes progressively more negative. Thus, the eigenvalue at the bottom right is associated with the fastest stable mode.

The above Schur decomposition, combined with the solution of a Sylvester equation allows the Jacobian to be written in the following form

$$\mathbf{G_Y} = (\ \mathbf{Z}_S \quad \mathbf{Z}_F\ )\begin{pmatrix} \mathbf{N}_S & 0 \\ 0 & \mathbf{N}_F \end{pmatrix}\begin{pmatrix} \hat{\mathbf{Z}}_S \\ \hat{\mathbf{Z}}_F \end{pmatrix} \qquad \text{with} \qquad \begin{pmatrix} \hat{\mathbf{Z}}_S \\ \hat{\mathbf{Z}}_F \end{pmatrix} = (\ \mathbf{Z}_S \quad \mathbf{Z}_F\ )^{-1}. \tag{15}$$

Here $\mathbf{Z}_S$ has M column vectors, each of length $N - L$, which span the subspace associated with the M slow time scales. Further, $\mathbf{Z}_F$ has $N - L - M$ column vectors, each of length $N - L$, which span the subspace associated with the $N - L - M$ fast time scales. The matrices $\hat{\mathbf{Z}}_S$ and $\hat{\mathbf{Z}}_F$, as defined in Equation (15), have dimension $M \times (N - L)$ and $(N - L - M) \times (N - L)$, respectively, and are associated with the reciprocal slow and fast basis vectors. The matrix $\mathbf{N}_S$ has dimension $M \times M$, is upper-triangular, and has as its eigenvalues those associated with the slow time scales. The matrix $\mathbf{N}_F$ has dimension $(N - L - M) \times (N - L - M)$, is upper-triangular, and has as its eigenvalues those associated with the fast time scales.

6

For fixed energy, density, and element mass fractions, the ILDM method identifies M-dimensional subspaces ($M < N - L$) on which slower time scale events evolve. An ILDM which equilibrates the $N - L - M$ fast time scales and consequently describes the M-dimensional manifold is given by

$$\hat{\mathbf{Z}}_F \cdot \mathbf{G}(\mathbf{Y}) = 0, \tag{16}$$

which forms $N - L - M$ algebraic equations. For what is effectively a complicated one-step chemistry, we take $M = 1$.

To construct the manifold for fixed energy, density, and element mass fractions, one first determines the equilibrium point of the system, which is taken as the original seed value. In subsequent calculations, the most recently calculated point is used as the seed value. One then performs the local fast and slow subspace decomposition, which gives local eigenvalues and associated basis vectors for a system linearized about the seed value. One then perturbs $N - L$ of the species away from their seed values in a prescribed manner to form the M algebraic equations below:

$$\mathbf{P} \cdot (\mathbf{Y} - \mathbf{Y}_o) = \boldsymbol{\delta}. \tag{17}$$

Here $\mathbf{P}$ is a user-specified parameterization matrix of dimension $M \times (N - L)$, $\boldsymbol{\delta}$ is a vector of length M which contains a user-specified increment in the projected mass fractions, and $\mathbf{Y}_o$ is a vector of length $N - L$ which contains the seed values of mass fractions. These M equations are solved simultaneously with the $N - L - M$ algebraic ILDM equations (16) with a predictor corrector technique which uses a tangent predictor and a Newton's method corrector to obtain the mass fractions at a new point on the manifold. The process is repeated to construct the global ILDM. We adapt the parameterization matrix $\mathbf{P}$ to overcome difficulties associated with turning points of the manifold in composition space. The choice of $\mathbf{P}$ is based on a continuation method which is an extrapolation of previous points of the ILDM used to estimate the location of the new points. This method can also be used for computing manifolds for an adiabatic, isobaric system.

With this analysis, an M-dimensional manifold can be identified in an $(N - L)$-dimensional composition space for a given set of ρ_o, e_o, $y_{1_o}, \ldots, y_{(L-1)_o}$. Thus, a different ILDM is required for a different set of densities, internal energies and element mass fractions. Since in general calculations one can expect all of these quantities to vary, the actual relevant reaction manifold which must be formed has dimension $K = M + 1 + L$ and can be tabulated numerically to give

$$Y_i = Y_i(Y_1, \ldots, Y_M, e, \rho, y_1, \ldots, y_{L-1}) \qquad \text{for} \qquad i = M + 1, \ldots, N - L, \tag{18}$$

where $Y_1, \ldots, Y_M$ are the chosen reference variables for the ILDM lookup table. The reference variables are chosen in such a way that the ILDM is single valued with respect to these variables for easy lookup. While there is no guarantee of single-valuedness, in the problems studied we have found it to be the case.

It is the dimension of the lookup table, K, which is critically important in manifold methods. Many previously reported calculations have been restricted to premixed conditions in the isobaric and/or adiabatic limits, thus reducing the dimension K. In the calculations presented here, variable energy and density are intrinsic features of the flow; given that we have chosen $M = 1$ for the hydrogen/oxygen/argon system discussed later ($L = 3$) we in principle must deal with a table which has dimension $K = 5$. Because we will study a uniformly premixed mixture, and because we employ a simplified diffusion model in which there is no preferential diffusion, $L - 1 = 2$ independent element mass fractions remain constant throughout the calculations, reducing the effective dimension of the manifold to $K = 3$. The variables of manifold parameterization for our hydrogen/argon/oxygen problem are chosen to be e, ρ, and Y_{H_2O}. In the ignition delay problem considered later for a mixture of hydrogen/ oxygen/argon, we use a 9 species 37 step reaction mechanism described in Table 1. With $M = 1$, a projection of the ILDM for fixed internal energy, density, (as well as the always fixed element mass fractions), for this system is plotted in Fig. 1 with Y_{H_2O} used as the reference independent variable for the ILDM and $Y_{H_2O_2}$ as the dependent variable. Mass fractions for all species (not shown here) are also available as functions of Y_{H_2O} for the same fixed internal energy and density. Also shown on the plot are projections of trajectories in this two-dimensional subspace for a variety of initial conditions. It is seen that all trajectories relax to the ILDM. As indicated on Fig. 1, the relaxation from the initial state to the manifold occurs on a relatively fast time scale on the order of microseconds, while once on the ILDM, the subsequent relaxation to final equilibrium occurs on a much slower time scale

7

j	Reaction	a_j	β_j	E_j
1	$O_2 + H \to OH + O$	2.00×10^{14}	0.00	70.30
2	$OH + O \to O_2 + H$	1.46×10^{13}	0.00	2.08
3	$H_2 + O \to OH + H$	5.06×10^{4}	2.67	26.30
4	$OH + H \to H_2 + O$	2.24×10^{4}	2.67	18.40
5	$H_2 + OH \to H_2O + H$	1.00×10^{8}	1.60	13.80
6	$H_2O + H \to H_2 + OH$	4.45×10^{8}	1.60	77.13
7	$OH + OH \to H_2O + O$	1.50×10^{9}	1.14	0.42
8	$H_2O + O \to OH + OH$	1.51×10^{10}	1.14	71.64
9	$H + H + M \to H_2 + M$	1.80×10^{18}	-1.00	0.00
10	$H_2 + M \to H + H + M$	6.99×10^{18}	-1.00	436.08
11	$H + OH + M \to H_2O + M$	2.20×10^{22}	-2.00	0.00
12	$H_2O + M \to H + OH + M$	3.80×10^{23}	-2.00	499.41
13	$O + O + M \to O_2 + M$	2.90×10^{17}	-1.00	0.00
14	$O_2 + M \to O + O + M$	6.81×10^{18}	-1.00	496.41
15	$H + O_2 + M \to HO_2 + M$	2.30×10^{18}	-0.80	0.00
16	$HO_2 + M \to H + O_2 + M$	3.26×10^{18}	-0.80	195.88
17	$HO_2 + H \to OH + OH$	1.50×10^{14}	0.00	4.20
18	$OH + OH \to HO_2 + H$	1.33×10^{13}	0.00	168.30
19	$HO_2 + H \to H_2 + O_2$	2.50×10^{13}	0.00	2.90
20	$H_2 + O_2 \to HO_2 + H$	6.84×10^{13}	0.00	243.10
21	$HO_2 + H \to H_2O + O$	3.00×10^{13}	0.00	7.20
22	$H_2O + O \to HO_2 + H$	2.67×10^{13}	0.00	242.52
23	$HO_2 + O \to OH + O_2$	1.80×10^{13}	0.00	-1.70
24	$OH + O_2 \to HO_2 + O$	2.18×10^{13}	0.00	230.61
25	$HO_2 + OH \to H_2O + O_2$	6.00×10^{13}	0.00	0.00
26	$H_2O + O_2 \to HO_2 + OH$	7.31×10^{14}	0.00	303.53
27	$HO_2 + HO_2 \to H_2O_2 + O_2$	2.50×10^{11}	0.00	-5.20
28	$OH + OH + M \to H_2O_2 + M$	3.25×10^{22}	-2.00	0.00
29	$H_2O_2 + M \to OH + OH + M$	2.10×10^{24}	-2.00	206.80
30	$H_2O_2 + H \to H_2 + HO_2$	1.70×10^{12}	0.00	15.70
31	$H_2 + HO_2 \to H_2O_2 + H$	1.15×10^{12}	0.00	80.88
32	$H_2O_2 + H \to H_2O + OH$	1.00×10^{13}	0.00	15.00
33	$H_2O + OH \to H_2O_2 + H$	2.67×10^{12}	0.00	307.51
34	$H_2O_2 + O \to OH + HO_2$	2.80×10^{13}	0.00	26.80
35	$OH + HO_2 \to H_2O_2 + O$	8.40×10^{12}	0.00	84.09
36	$H_2O_2 + OH \to H_2O + HO_2$	5.40×10^{12}	0.00	4.20
37	$H_2O + HO_2 \to H_2O_2 + OH$	1.63×10^{13}	0.00	132.71

Table 1: Nine species, thirty-seven step reaction mechanism for hydrogen/oxygen/argon mixture, Maas and Warnatz, 1988, with corrected f_{H_2} from Maas and Pope, 1992, also utilized by Fedkiw, *et al.*, 1997. Units of a_j are in appropriate combinations of cm, mol, s, and K so that $\dot{\omega}_i$ has units of $mol\ cm^{-3}\ s^{-1}$; units of E_j are $kJ\ mol^{-1}$. Third body collision efficiencies with M are $f_{H_2} = 1.00$, $f_{O_2} = 0.35$, and $f_{H_2O} = 6.5$.
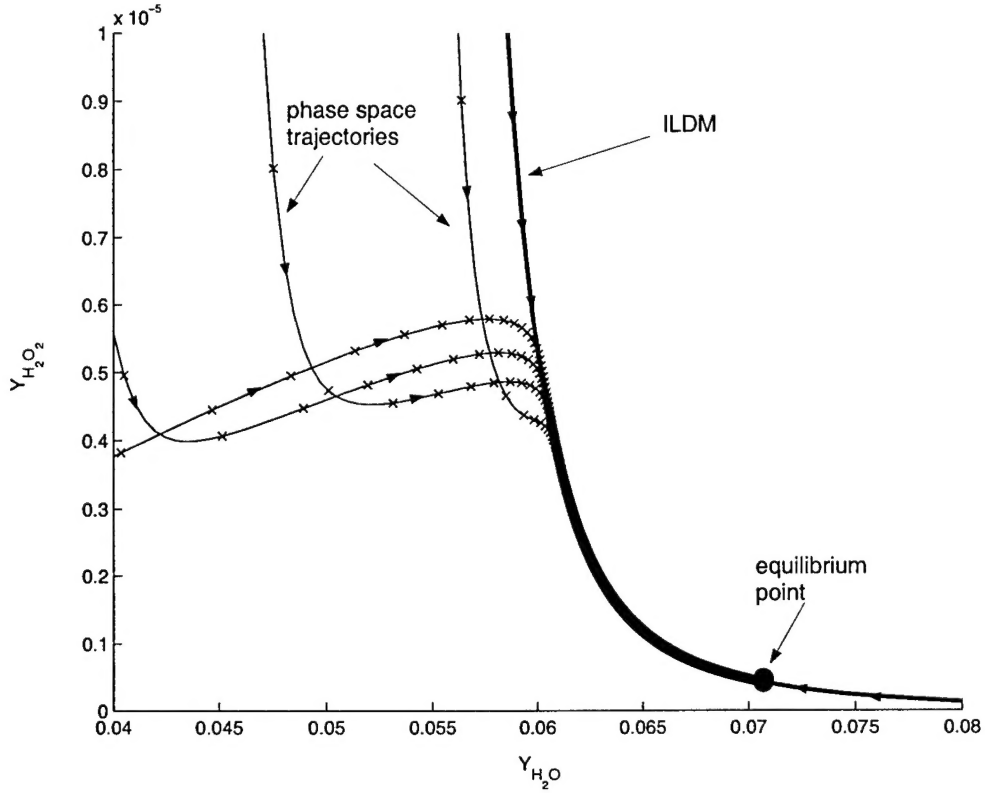
Figure 1: ILDM projection for 9 species 37 step reaction mechanism of hydrogen/oxygen/argon combustion as function of Y_{H_2O} at constant values of $\rho = 0.5$ kg m^{-3}, $e = 8.0 \times 10^5$ J kg^{-1}. Element mass fractions fixed at $y_H = 0.01277$, $y_O = 0.10137$, $y_{Ar} = 0.88586$. Also plotted are trajectories from full time integration showing relaxation to the manifold and equilibrium. The symbol 'x' denotes equally spaced 0.10 μs time intervals. Total time to relax to equilibrium is near 0.1 ms.

on the order of 0.1 ms. The phase trajectories appear to cross, but this is because they have been projected into a lower dimensional space.

A projection of the $K = 3$ ILDM for constant density and the same constant element mass fractions for the hydrogen/oxygen/argon system is plotted in Fig. 2, with Y_{H_2O} and e used as the reference independent variables and $Y_{H_2O_2}$ as the dependent variable. The portion of the ILDM depicted closely corresponds to values realized in the ignition delay problem discussed later. Also, for the system studied here, the dependency of all variables on density was weak for the range of realized density values.

Equation (13) can be solved using the ILDM method if the composition of the mixture at a given spatial point is close to the ILDM. One illustrative way to achieve this is to locally project Equation (13) onto the slow subspace:

$$\hat{\mathbf{Z}}_S \cdot \frac{d}{dt}\mathbf{Y} = \hat{\mathbf{Z}}_S \cdot \mathbf{G}(\mathbf{Y}). \tag{19}$$

This results in M ordinary differential equations and models the dynamics of reduced chemistry. In practice, we simply integrate M of the species equations in their original form while using the manifold to obtain all necessary secondary variables.

When using ILDMs with $M = 1$, we need to integrate only one differential equation associated with the reference variable at each spatial location. If the composition is far from the ILDM, it is important to incorporate the off-manifold kinetics in some fashion. Here the full reaction kinetic equations are integrated using LSODE in implicit mode. We switch from full integration to the ILDM method when the L_2 norm
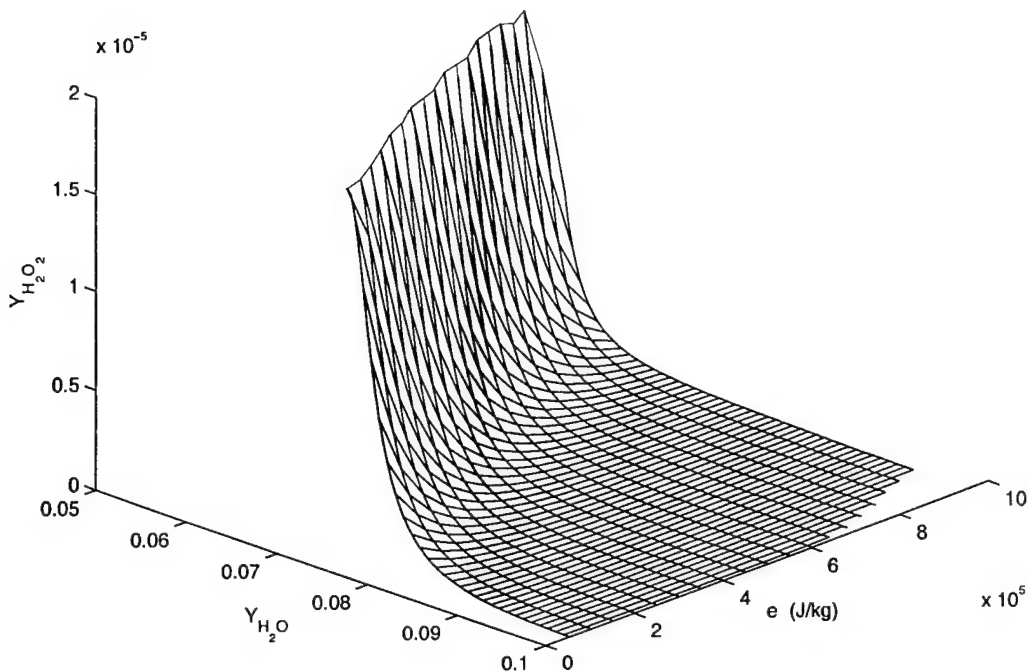
9

Figure 2: ILDM projection for 9 species 37 step mechanism of hydrogen/oxygen/argon combustion giving $Y_{H_2O_2}$ as a function of Y_{H_2O} and e for constant $\rho = 0.5\ kg\ m^{-3}$. Element mass fractions fixed at $y_H = 0.01277$, $y_O = 0.10137$, $y_{Ar} = 0.88586$.

between the actual mass fractions at a particular location and the corresponding projected mass fractions is less than 1×10^{-6}. While this reduces the efficacy of the ILDM method, it is critical to avoid large phase errors associated with projecting onto the manifold from a remote region of phase space. In other words, while all processes are typically destined to reach the manifold, it is critical for the proper sequencing of events that they reach the manifold at the correct time, and reach the right point on the manifold. A naive projection can easily give plausible answers which have $O(1)$ errors associated with them. In practice, in our calculations for the ignition delay problem, we find we are able to use the ILDM method in cells which have recently been shocked, have passed through the bulk of the induction zone, and are well within the thermal explosion region. The ILDM method is also applied to points in the trailing rarefaction wave.

The convection-diffusion step is equivalent to a perturbation off the ILDM. Subsequent to the perturbation, there is a fast relaxation to the manifold corresponding to a new set of conserved variables. This is accomplished here by projection onto the manifold while holding the reference variable, here Y_{H_2O}, constant. This projection is allowed by the large time scale difference between slow chemical/fluid time scales and fast chemical time scales as long as convective and diffusive effects are not large. We also note that for this hydrogen/oxygen/argon mechanism the fast directions are nearly orthogonal to the slow variable, Y_{H_2O}, on the ILDM. A slightly more accurate alternative would be to project to the manifold in the direction of the vectors associated with the fast eigenmodes. In contrast to many implementations of the ILDM method for partial differential equations, which are often confined to a single adiabatic, isobaric ILDM, we convect and diffuse all variables, not just slow variables associated with the ILDM. While this comes at a cost of solving more equations, it is necessary to preserve the consistency of the Strang operator splitting method.

Alternatively, for our problem, which is neither adiabatic, isobaric, or isochoric, we could choose to incur the extra expense of tabulating the slow and fast subspaces associated with changes in energy and density and then convect and diffuse just slow variables.

5 Wavelet Adaptive Multilevel Representation (WAMR)

Much of the material of this section builds on Vasilyev and Paolucci, 1995, 1996, 1997 and is described more fully in Rastigejev and Paolucci, 1999, 2002.

5.1 Bases and Wavelet Approximation

Wavelet analysis is a new numerical concept (*cf.* Daubechies, 1992; Meyer, 1990), which allows one to represent a function in terms of basis functions, called wavelets, which are localized in both location and scale. The Daubechies autocorrelation functions and boundary-modified Daubechies autocorrelation functions (see Saito and Beylkin, 1993) of order p have been used as elements for the construction of basis functions. If $\varphi(x)$ is the Daubechies scaling function of order p (p coefficients in the dilatation equation and corresponding to $p/2$ vanishing moments) then $\phi(x) = \int_{-\infty}^{+\infty} \varphi(y - x)\varphi(y)dy$ is the Daubechies autocorrelation function of order p having p vanishing moments. In addition, following Donoho, 1992, we use the following definition for the wavelet:

$$\psi(x) = \phi(2x - 1). \tag{20}$$

For this wavelet basis, the algorithm for finding wavelet expansion coefficients reduces to the use of simple Lagrange interpolation (see Saito and Beylkin, 1993, and Dubuc, 1986).

Now any continuous function $f(x)$ defined in a finite domain may be approximated within a prescribed accuracy (for L large enough) by

$$\mathbf{P}^L f(x) = \sum_k f_k \phi(x - k) + \sum_{l=0}^{L} \sum_k d_{l,k} \psi(2^l x - k). \tag{21}$$

Left and right boundary-modified scaling functions can be constructed to span the finite domain but we do not write them here (see Rastigejev and Paolucci, 1999).

5.2 Sparse Wavelet Approximation and Irregular Grid

The spatially adaptive collocation grid is especially well tailored for strongly time-dependent problems. The method incorporates the dynamically adaptive multilevel algorithm of Liandrat and Tchamitchian, 1990. The adaptation is achieved by retaining only those wavelets whose amplitudes are greater than a given threshold. Thus, high resolution computations are carried out only in those regions where sharp transitions occur. In order to make the wavelet approximation of a function efficient (*i.e.* to use the smallest possible number of wavelet modes) while at the same time retaining the accuracy of the representation, we introduce the sparse wavelet representation by thresholding the wavelet coefficients. The approximation can be split into two parts which are composed of wavelets whose amplitudes are above and below a specified threshold ϵ:

$$\mathbf{P}^L f(x) = \mathbf{P}^L_{\geq} f(x) + \mathbf{P}^L_{<} f(x), \tag{22}$$

where

$$\mathbf{P}^L_{\geq} f(x) = \sum_k f_{0,k} \phi_{0,k}(x) + \sum_{l=0}^{L} \sum_{k, |d_{l,k}| \geq \epsilon} d_{l,k} \psi_{l,k}(x), \tag{23}$$

$$\mathbf{P}^L_{<} f(x) = \sum_{l=0}^{L} \sum_{k, |d_{l,k}| < \epsilon} d_{l,k} \psi_{l,k}(x). \tag{24}$$

11

We now call $\mathbf{P}_{\geq}^{L} f(x)$ the sparse wavelet representation of the function $f(x)$, and we call the corresponding wavelets used in the representation *essential wavelets*. In this representation, if a wavelet is omitted, so is the corresponding collocation point. This compression results in the irregular grid $G_{\geq}$.

5.3   Time Integration Algorithm

After the operator splitting and application of the wavelet discretization in space, Equation (11) reduces to a system of ordinary differential equations (ODEs):

$$\frac{d\mathbf{u}}{dt} = \mathbf{F}(\mathbf{u}), \tag{25}$$

where $\mathbf{u}$ is a vector of dependent variables defined on the nonuniform collocation grid, and $\mathbf{F}$ represents the discretization of the convection and diffusion terms. Spatial derivatives are approximated by use of the Lagrange polynomial corresponding to the wavelet basis evaluated at collocation points.

To integrate this system, we use the linearized trapezoidal method to obtain the following system of linear algebraic equations:

$$\mathbf{A}^{(n)}\Delta\mathbf{u}^{(n+1)} = \mathbf{b}^{(n)}, \tag{26}$$

where $\mathbf{A}^{(n)} = \left(\mathbf{I} - \frac{\Delta t}{2}\mathbf{J}^{(n)}\right)$, $\Delta\mathbf{u}^{(n+1)} = \mathbf{u}^{(n+1)} - \mathbf{u}^{(n)}$, $\mathbf{b}^{(n)} = \frac{\Delta t}{2}\left[\mathbf{F}\left(t^{(n+1)}, \mathbf{u}^{(n)}\right) + \mathbf{F}\left(t^{(n)}, \mathbf{u}^{(n)}\right)\right]$, $\mathbf{I}$ is the identity matrix and $\mathbf{J} = \partial\mathbf{F}/\partial\mathbf{u}$ is the Jacobian matrix.

In order to take advantage of the sparseness of matrix $\mathbf{A}^{(n)}$, as well as the fact that $\Delta\mathbf{u}^{(n+1)}$ is small, the system of algebraic equations is solved by using a multiscale Schwarz-type domain-decomposition method which utilizes a multigrid-type iteration cycle for solving the above linear problem. First the hierarchy of grids are projected to the physical domain and they are subsequently decomposed into multiple disjoint subsets consisting of grids of different size as shown in Figure 3. The next step consists of the solution of

Figure 3: Iteration procedure.

the linear system on these disjoint domains using a multigrid-type iteration cycle on every subset (linear subsystem). Since the problem is often stiff on the finer grids, the GMRES method is used as the basic iteration algorithm (see Saad and Schultz, 1986). The method has potential for additional development and improvement.

A typical cycle is illustrated in Figure 4 where G_1 and G_4 correspond to the finest and coarsest grid subsets, respectively. The number of unknowns in each subset is approximately the same, so that in this example each subset would contain approximately one-fourth of the total number of grids. Typically the cycle starts from the finest grid subset. The residual tolerance is decreased on every successive branch of the cycle. We note that the number of iterations required to satisfy the tolerance drops rapidly. To improve the performance, a reasonable (but not very accurate) initial guess of the solution is used. Two alternatives have been tried. In one, the initial guess is obtained by solving exactly the linear tridiagonal system resulting from a three point finite-difference derivative spatial approximation. In the other, we use the initial guess

$$\Delta\mathbf{u}^{(n+1)} = \begin{cases} \Delta\mathbf{u}^{(n)}, & \text{if the grid has not changed,} \\ I\left(\Delta\mathbf{u}^{(n+1)}\right), & \text{if the grid has changed,} \end{cases} \tag{27}$$

where we define $\Delta\mathbf{u}^{(0)} = \mathbf{0}$, and I is the wavelet interpolation operator which interpolates from the nonuniform old grid to the nonuniform new grid.
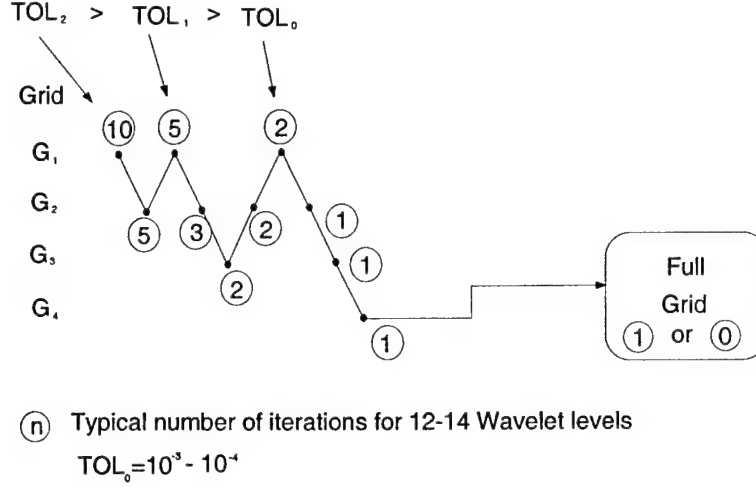
5.4   Dynamically Adaptive Algorithm

Figure 4: Iteration procedure.

In order to resolve all structures appearing in the solution of the problem as time evolves, we need to adapt the sparse wavelet representation in time. To accomplish this, at any time we need to save the amplitudes of essential wavelets and the amplitudes of wavelets in the *neighboring region, i.e.* those wavelets which are near the essential wavelets in location and scale. Essential and neighboring wavelets constitute the group of *active wavelets*. The irregular grid $G_\geq$ is composed of collocation points corresponding to all active wavelets at any given moment of time.

The numerical algorithm for solving the system of ODEs may be summarized as follows:

1. integrate the ODEs to obtain the approximate solution $\mathbf{u}^{(n+1)}$ on the irregular grid $G_\geq^{(n)}$ by using $\mathbf{u}^{(n)}$ as initial conditions;

2. obtain the new grid $G_\geq^{(n+1)}$ based on the magnitudes of wavelet coefficients of $\mathbf{u}^{(n+1)}$ and accounting for the new neighboring region;

3. if $G_\geq^{(n+1)} = G_\geq^{(n)}$ we increment time and go back to step 1, otherwise compute the values of $\mathbf{u}^{(n+1)}$ at the new collocation points in $G_\geq^{(n+1)}$, then increment time and go back to step 1.

The dynamically adaptive wavelet collocation algorithm is ideally suitable for handling problems with localized structures, which might occur intermittently anywhere in the computational domain or change their locations and scales in space and time. The implementation of conventional adaptive algorithms is very costly due to the possibility of grids varying drastically within a short time interval. The use of conventional algorithms on a uniform grid is impractical. Thus, the main advantage of the dynamically adaptive wavelet collocation algorithm is that it requires a far fewer number of unknowns than the other algorithms, when applied to problems with a great range of spatial scales. In addition, the computational grid can be refined locally to an arbitrary small size. We emphasize here that the adaptation of the computational grid does not require additional efforts and consists merely in turning on and off wavelets at different locations and scales. Moreover, the algorithm exhibits an exponential convergence on the unevenly spaced mesh. The computational cost is independent of the spatial dimensionality and is $O(\mathcal{N})$, where $\mathcal{N}$ is the total number of collocation points. This computational efficiency is possible by virtue of the Fast Wavelet Collocation Transform (see Vasilyev and Paolucci, 1997). Another important property of the algorithm is that the relative error is actively controlled by prescribing a resolution threshold parameter. All of these features make this algorithm a very attractive candidate for tough combustion problems.

13

6   Results

We describe here two representative problems that highlight the strengths of the WAMR/ILDM algorithm. In the first subsection we discuss in detail a one-dimensional reactive flow with realistic chemistry. In the second, we give a briefer discussion of results from a benchmark two-dimensional problem at large Reynolds numbers.

6.1   Ignition delay in a shock tube

We describe the classical hydrogen-oxygen-argon shock tube ignition delay problem. This is a common benchmark problem for both experiments and computations. Here we consider an extension to the well-documented case considered by Fedkiw, *et al.*, 1997, and fully described by Singh, *et al.*, 2001. We consider a shock tube of length $0.12\ m$ filled initially with H_2, O_2, and Ar in a 2/1/7 molar ratio. For $0 \leq x \leq 0.06\ m$, the gas is taken to be at $\rho = 0.18075\ kg\ m^{-3}$, $u = 487.34\ m\ s^{-1}$, and $p = 35.594\ kPa$. For $0.06 < x \leq 0.12\ m$, the gas is at $\rho = 0.072\ kg\ m^{-3}$, $u = 0\ m\ s^{-1}$, and $p = 7.173\ kPa$. This state is consistent with Rankine-Hugoniot jump conditions for the inviscid equivalent of Equation (6). Knowledge of these parameters allows determination of all other dependent variables at $t = 0\ s$ through the use of the governing equations. At $x = 0.12\ m$, we consider a boundary which is closed and adiabatic. Consequently $u = 0\ m\ s^{-1}$, and additionally diffusive mass and energy fluxes J_n^m $(n = 1, \ldots, N)$, and J^q must be zero. At $x = 0\ m$, we allow inflow conditions of $u = 487.34\ m\ s^{-1}$, $\rho = 0.18075\ kg\ m^{-3}$, $p = 35.594\ kPa$. The lead shock wave is of insufficient strength to ignite the material on time scales of interest. When the lead shock encounters a wall, a stronger shock reflects, and leaves the mixture at a sufficiently elevated temperature so that reaction soon ensues. After a brief ignition delay, significant reaction commences at the reflecting wall, generating a detonation wave which overtakes the reflected shock. Fedkiw, *et al.*, 1997, model this process with one-dimensional reactive Euler equations, assuming a mixture of ideal gases with variable specific heats are reacting in a thirty-seven step reaction mechanism in the presence of nine species.

We have first reproduced Fedkiw, *et al.*'s, 1997, results using an identical model and technique. It is a simple step to extend these results to incorporate the ILDM technique. We have generated ILDMs for the entire range of energies and densities encountered in this problem. Additionally, we have extended the model to include the effects of mass, momentum and energy diffusion and generated results using the WAMR technique for spatial discretization. Use of the ILDM closely replicates the full solution.

Results for the shock tube calculations are given here. Figure 5 gives predictions of temperature, velocity, pressure, and density vs. distance at time $t = 195\ \mu s$. At this time, the lead right-traveling inert shock has reflected off the right wall and is propagating to the left with its head near $x = 0.065\ m$ at a pressure and temperature of $118.8\ kPa$ and $1196\ K$, respectively. Close behind the lead shock is the much stronger, left-propagating ZND detonation wave, with its head near $x = 0.072\ m$. All of the usual salient features of a ZND detonation are predicted here. The von Neumann spike is predicted at a pressure of around $450\ kPa$, and the pressure relaxes to near $200\ kPa$ at the right boundary. The post-detonation temperatures are near $2500\ K$, and the velocity is seen to relax to a value of zero at the right boundary.

The solid lines show the predictions of the full chemical kinetics model. The dots show the results of the calculations using the ILDM resolving one reaction time scale; this can be interpreted as one-step chemistry with a rational fidelity to full chemical kinetics. It is seen on this scale that the predictions are nearly identical! Examination of the local eigenvalues indicates that use of the manifold suppresses temporal resolution of reaction events which occur faster than a roughly $0.1\ \mu s$ time scale. For a given ρ and e, we construct the ILDM using adaptive parameterization as described by Maas, 1998. This is done for sixteen values of ρ ranging from $0.25\ kg\ m^{-3}$ to $1.00\ kg\ m^{-3}$ in steps of $0.05\ kg\ m^{-3}$. Similarly we use nineteen values of e ranging from $0.5 \times 10^5\ J\ kg^{-1}$ to $9.5 \times 10^5\ J\ kg^{-1}$ in steps of $0.5 \times 10^5\ J\ kg^{-1}$. Hence 304 slices such as shown in Figure 1 were constructed. Finally each ILDM was stored with an equally spaced parameterization of 100 values of Y_{H_2O} for easy lookup. Thus, the ILDM lookup table has a size of $16 \times 19 \times 100$.

The effects of diffusion are clearly seen when one examines finer length scales. Figure 6 shows two views of pressure vs. distance at a somewhat later time, $t = 230\ \mu s$, by which time the detonation wave has overtaken the reflected shock. In the view on the left, the same length scale is shown as in Fig. 5. The view on the right shows a 120 factor spatial magnification near the lead shock. In this figure the dots represent the actual collocation points as chosen by the WAMR technique. It has been found that fifteen levels of
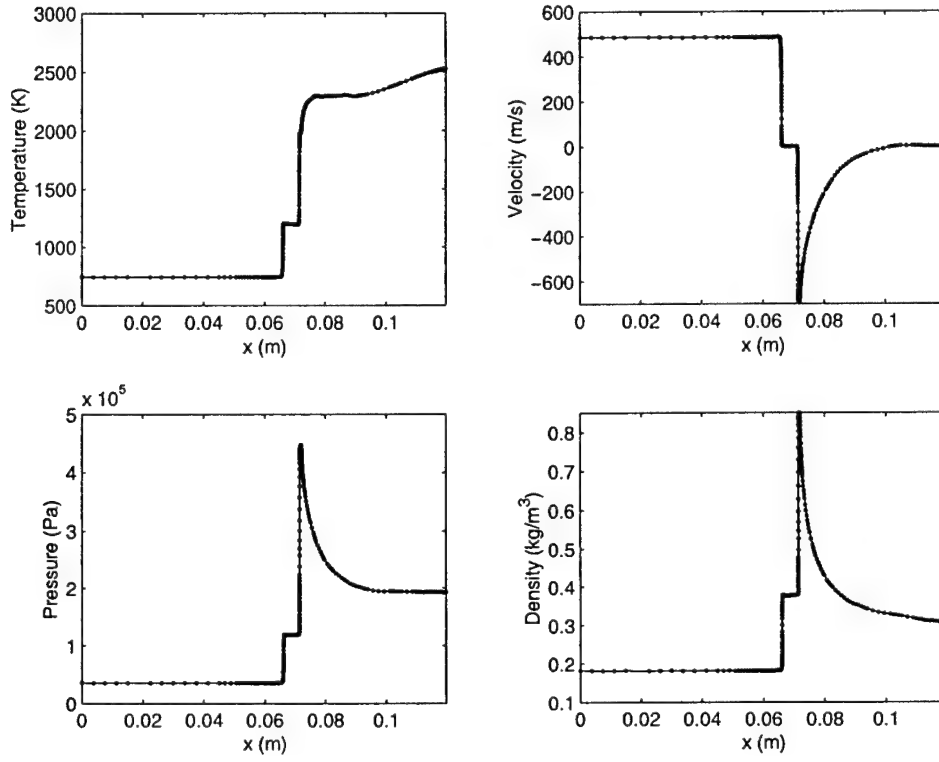
Figure 5: Predictions of temperature, velocity, pressure, and density vs. distance at $t = 195 \ \mu s$ using a maximum of 300 collocation points, 15 scale levels for full chemical kinetics (solid lines) and ILDM kinetics (dots) for viscous hydrogen/oxygen/argon detonation.
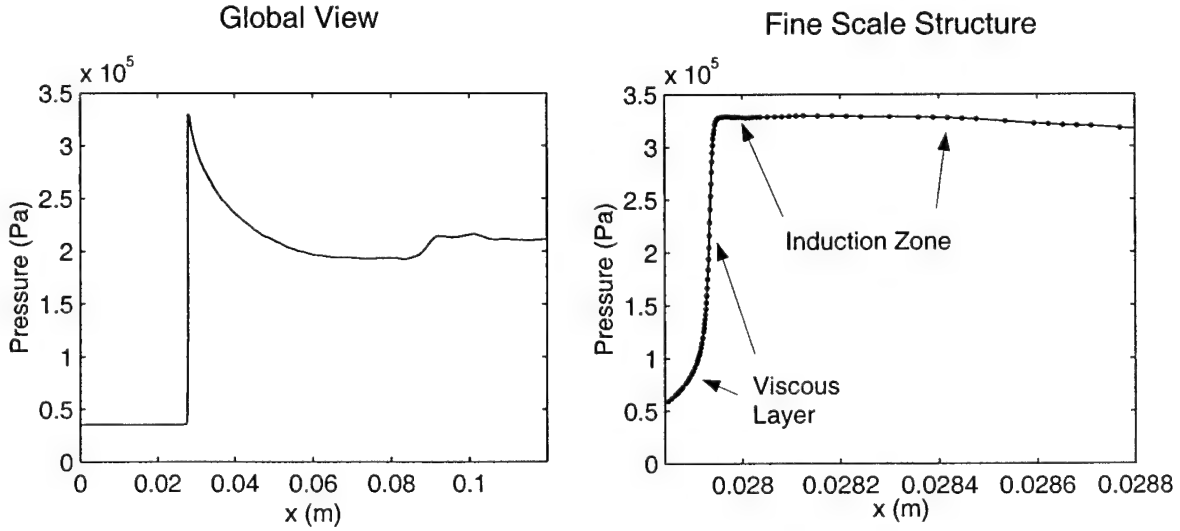

Figure 6: Predictions of pressure vs. distance for $H_2/O_2/Ar$ ignition delay at $t = 230 \ \mu s$ on coarse and fine length scales demonstrating the spatial resolution of viscous and induction zone structures.

wavelets (equivalent to 2^{15} uniform grids) are sufficient to achieve the desired accuracy. Moreover, because of the adaptive nature of the method, only three hundred collocation points at most are necessary to achieve this detail! It is clear on this scale that both the viscous shock and chemical induction zones have been resolved. Here it is predicted that the shock is essentially inert and has a thickness of roughly 50 μm.

The induction zone, a region of essentially constant pressure, temperature, and density, has a thickness of roughly 470 μm. In the induction zone many reactions are actively occurring, giving rise to a release of energy which, because of the extreme temperature sensitivity of reaction rates, accumulates to an extent that a thermal explosion occurs at the end of the induction zone. While the wavelet representation certainly has captured these thin layers, it is noted that because it was chosen not to use individual species mass fractions as part of the adaption criteria, some finer scale reaction zone structures have not been spatially resolved.

In the process of understanding the time scales associated with the kinetics of a spatially homogeneous mixture, we have computed all time scales through an eigenvalue analysis. This analysis indicates that reaction time scales as small as sub-nanosecond are predicted by the standard models of Maas and Warnatz, 1988, and Maas and Pope, 1992. Such small time scales give rise to small reaction-induced spatial scales which violate the continuum assumption. It is essentially for this reason that we are not adapting our spatial grid to capture the subsequent extremely fine length scales associated with individual species mass fraction variation. This issue is pervasive in most calculations involving detailed chemical kinetics, but it is not often addressed since standard spatial discretization algorithms are unable to resolve this range of scales.

For this particular problem, use of the full integration technique requires three times as much computational time as the ILDM technique. We note however that general conclusions regarding computational efficiency are difficult to draw as the savings realized will be model-dependent as well as initial condition-dependent. The bulk of our savings are realized as more and more cells become chemically activated. At the beginning of the calculation, when most cells are in a cold state far from equilibrium, there is no savings. The calculation itself took roughly ten hours on a 330 MHz Sun Ultra10 workstation.

Figure 7 shows results for the species mass fractions at $t = 195$ μs. Steep gradients in mass fractions are predicted near the detonation front. As expected, HO_2, H, and H_2O_2 mass fractions have relatively small values which peak at the detonation front. Under these conditions, the major product is H_2O. On the length scales shown in Figs. 5 and 7, the results appear very similar to the inviscid predictions of Fedkiw, *et al.*, 1997.

Figure 8 demonstrates the adaptive nature of the WAMR technique. It shows the distribution of collocation points and their scale levels, $2^{-j}, j = 0, \ldots, 14$, at two different times, first at $t = 180$ μs, when the lead shock and the approaching detonation are present, and later at $t = 230$ μs, after they have merged. In both cases, at most three hundred collocation points and fifteen wavelet scale levels were sufficient to capture the flow features to the prescribed dimensionless error tolerance of 10^{-3}. Moreover, it is clear that the algorithm adapts to the features of the flow.

As discussed by Menikoff, 1994, inviscid codes introduce pseudo-entropy layers near regions of wave-wave and wave-boundary interactions. These often appear as $O(1)$ anomalies in temperature and density near the wall in shock tube predictions. Figure 9 shows the results of our viscous calculation in a spatial zone near the wall just after shock reflection. On this scale, there is no apparent entropy layer near the wall.

A finer scale examination of the dependent variables, shown in Figure 10, reveals what is happening. It is evident from the temperature plot that there is a small entropy layer near the wall, here physically induced. The physical diffusion mechanisms rapidly smear the layer within a few microseconds. It may be possible that the correct capturing of a temperature-sensitive ignition event near a wall could be critically dependent on having the correct physics in the model. For the viscous calculation, a temperature rise of roughly 5 K is predicted. Performing a similar calculation with an inviscid Godunov-based model with first order upwind spatial discretization near regions of steep gradients using 400 evenly spaced grid points induces a temperature rise of nearly 20 K, which persists. It might be expected that numerical diffusion would dissipate this temperature spike. However, as detailed by LeVeque, 1992, the leading order numerical diffusion coefficient for such methods is proportional to the local fluid particle velocity. As the fluid particle velocity at the wall and in the region downstream of the reflected shock is zero, the effects of numerical diffusion here are at most, confined to higher order. This temperature rise, similar to that obtained by Fedkiw *et al.*, 1997, 1999, has been obtained by effectively imposing an adiabatic boundary condition done through extrapolation. This type of condition is inconsistent with the inviscid governing equations.
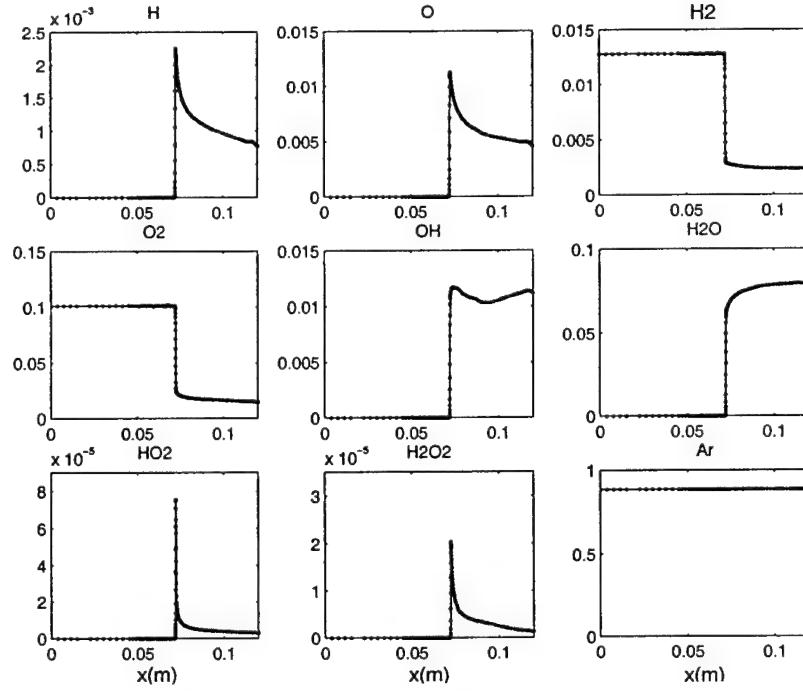
Figure 7: Predictions of species mass fractions vs. distance at $t = 195$ μs using a maximum of 300 collocation points, 15 scale levels for full chemical kinetics (solid lines) and ILDM kinetics (dots) for viscous hydrogen/oxygen/argon detonation.
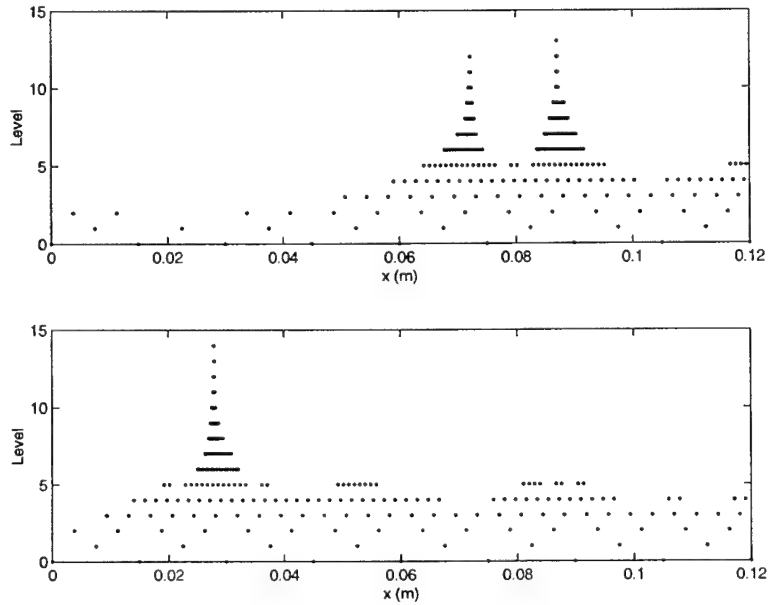

Figure 8: Spatial distribution of collocation points and levels at $t = 180$ μs (two shock structure) $t = 230$ μs (single shock structure) demonstrating grid adaption.
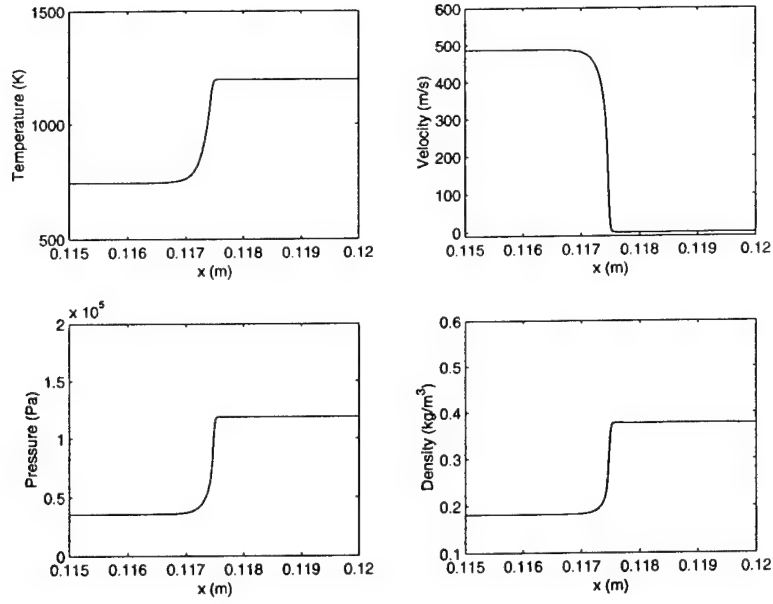
17

Figure 9: Predictions of temperature, velocity, pressure, and density vs. distance before commencement of significant reaction but after shock reflection using a reactive Navier-Stokes model, $t = 177 \ \mu s$.
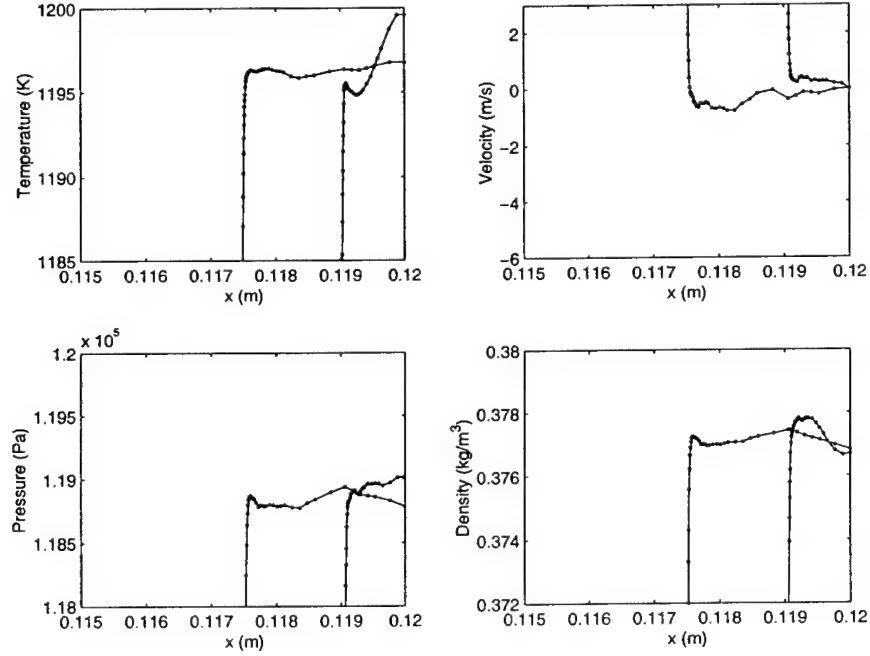

Figure 10: Close-up view of predictions of temperature, velocity, pressure, and density vs. distance before commencement of significant reaction but just after shock reflection ($t = 174 \ \mu s$) and slightly later ($t = 177 \ \mu s$).

6.2 Lid-driven cavity

Here results are presented for a standard benchmark flow using the WAMR algorithm: a lid-driven fluid in a square cavity. In this problem, a fluid is confined in a square cavity. Three of the walls are stationary, while one wall has a constant velocity. In order to satisfy the no-slip boundary condition at all surfaces, the fluid is driven into rotational motion. As the Reynolds number is increased, more and more complex structures of different scales are generated in the flow field; such a flow is thus a good candidate for study with the WAMR technique. We compare our results with the widely cited study of Ghia, *et al.*, 1982, who considered a finite difference solution of precisely the same problem using multigrid methods in which the finest grid was equivalent to a 257×257 uniformly spaced computational grid.

The dimensionless, unsteady, two-dimensional, incompressible Navier-Stokes equations are adopted as a model:

$$\frac{\partial u}{\partial x} + \frac{\partial v}{\partial y} = 0, \tag{28}$$

$$\frac{\partial u}{\partial t} + u\frac{\partial u}{\partial x} + v\frac{\partial u}{\partial y} = -\frac{\partial p}{\partial x} + \frac{1}{Re}\left(\frac{\partial^2 u}{\partial x^2} + \frac{\partial^2 u}{\partial y^2}\right), \tag{29}$$

$$\frac{\partial v}{\partial t} + u\frac{\partial v}{\partial x} + v\frac{\partial v}{\partial y} = -\frac{\partial p}{\partial y} + \frac{1}{Re}\left(\frac{\partial^2 v}{\partial x^2} + \frac{\partial^2 v}{\partial y^2}\right). \tag{30}$$

In these equations independent variables are Cartesian coordinates x and y, and time t. Dependent variables are x-velocity u, y-velocity v, and pressure p. The only parameter is the Reynolds number, Re.

In applying the WAMR technique to this problem, the dependent variables are projected onto a wavelet basis extended to two-dimensions. Many of the same techniques discussed for one-dimensional methods apply here as well, and will not be discussed. Because of the two-dimensional nature of the flow however, it was necessary to develop a robust computational algorithm for computing derivatives on a non-uniform stencil. Further, a fast Poisson solver was developed to solve for the elliptic equation for pressure that was necessary to solve at every time step. Dynamic memory allocation was utilized for fluctuating storage requirements.

Results at $Re = 10000$, the highest Reynolds number in the published literature for which results exist, are shown in Figures 11, 12, and 13, at early stages of the flow development, at $t = 4, 12, 100$, respectively. It is noted that the asymptotic flow is oscillatory. Each of these figures gives a plot of the velocity vector field. It is important here to highlight the transitory portion of the development so that the adaptive nature of the method can be observed. In these figures, a velocity vector is affixed to the location of each wavelet. Figure 11 shows a prominent starting vortex, and there is a high concentration of wavelets in regions of steep gradients of the flow. In all of the calculations reported, five wavelet levels have been utilized. The coarsest set of wavelets gives results equivalent to a 16×16 grid and the finest is equivalent to at 256×256 grid, and is an equivalent resolution as Ghia, *et al.*'s finest grid. Figure 12 gives a snapshot at a later time when the primary vortex has convected and diffused further into the cavity. Once again, it is obvious that the wavelet collocation points have adapted to the changing nature of the flow. Figure 13 shows results at a much later time. Here, careful examination (not shown here) reveals that recirculation zones in the corners have been predicted.

Results at a lower Reynolds number, $Re = 3200$, are shown in Figure 14. Because of the lower Reynolds number, the fluid has relaxed to a steady state at the depicted time of $t = 100$. Figure 15 depicts the u component of velocity as a function of y for $x = 0.5$. The results from the WAMR are in very good agreement with published results of Ghia, *et al.* Moreover, we believe our results are actually more accurate since Ghia *et al.* found it necessary to use upwind differencing for convective terms to stabilize the numerical computations. As is well known, the use of upwind differencing introduces numerical diffusion into the solution. Figure 16, similar to Figure 15, depicts the v component of velocity as a function of x for $y = 0.5$. Again the results are very close to those of Ghia, *et al.* at the scale shown in the figure.

7   Conclusion

The essential goals of this research project have been achieved. Significant progress has been made in the development of both the method of intrinsic low dimensional manifolds as well as the wavelet adaptive
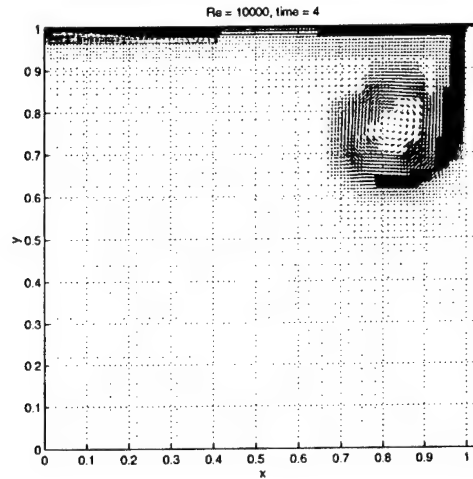
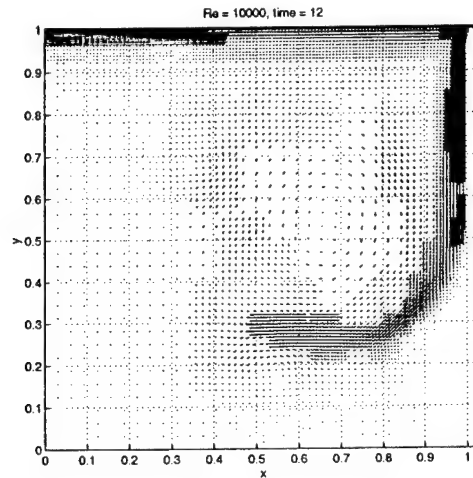Figure 11: Velocity vector field and collocation points for lid-driven cavity, $Re = 10000$, $t = 4$.

Figure 12: Velocity vector field and collocation points for lid-driven cavity, $Re = 10000$, $t = 12$.

multilevel representation algorithms. The methods have successfully been employed on challenging multiscale problems in reactive and multidimensional inert flows to predict results which have met or exceeded existing published standards.

The work is not incremental in character and in fact represents a substantially new approach which we believe has yielded consequent dividends. While additional generalizations can and should be made to the algorithm, we nevertheless believe the research has set a new standard in high performance computing applied to combustion. In addition we believe the combined novelty and utility of the WAMR/ILDM method will have ramifications extending into the other areas of computational physics.
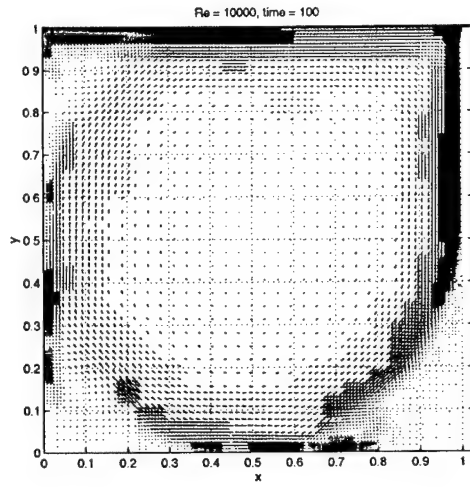
20

Figure 13: Velocity vector field and collocation points for lid-driven cavity, $Re = 10000$, $t = 100$.
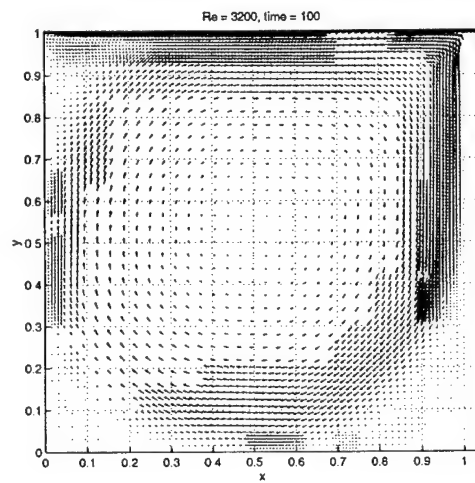

Figure 14: Velocity vector field and collocation points for lid-driven cavity, $Re = 3200$, steady state results.
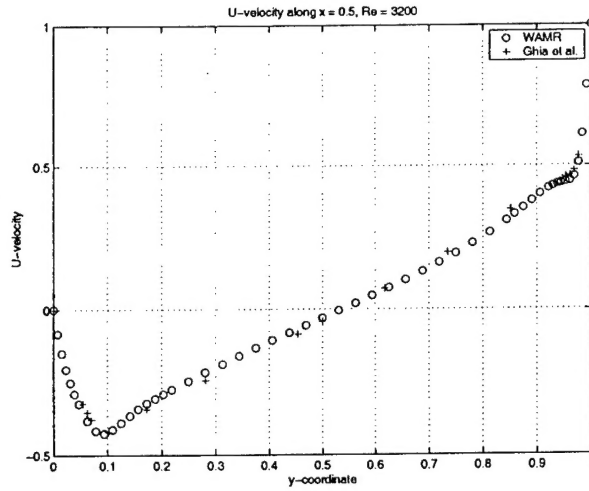
21

Figure 15: Comparison of midplane ($x = 1/2$) u with Ghia, *et al.*'s, 1982, results for lid-driven cavity at $Re = 3200$.
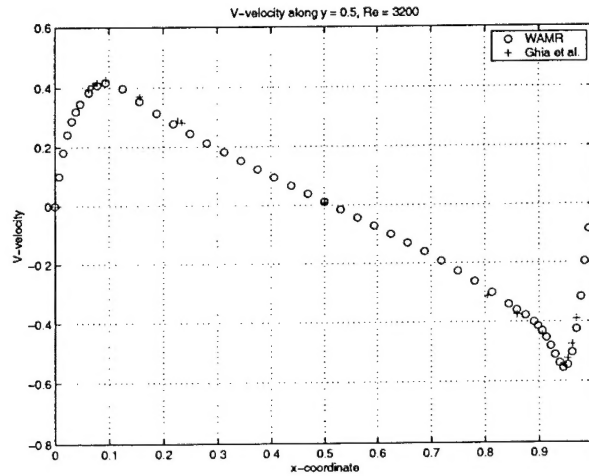

Figure 16: Comparison of midplane ($y = 1/2$) v with Ghia, *et al.*'s, 1982, results for lid-driven cavity at $Re = 3200$

8 Bibliography

Buckmaster, J. D., 1993, "The Structure and Stability of Laminar Flames," *Annual Review of Fluid Mechanics*, Vol. 25, pp. 21-53.

Buckmaster, J. D. and Ludford, G. S. S., 1982, *Theory of Laminar Flame*, Cambridge University Press: Cambridge.

Daubechies, I., 1992, *Ten Lectures on Wavelets*, CBMS-NSF Series in Applied Mathematics, Society of Industrial and Applied Mathematics: Philadelphia.

Donoho, D. L., 1992, "Interpolating Wavelet Transforms," Technical Report 408, Dept. of Statistics, Stanford University.

Dubuc, S., 1986, "Interpolation Through an Iterative Scheme," *Journal of Mathematical Analysis and Applications*, Vol. 114, No. 1, pp. 185-204.

Eggles, R. L. G. M., and DeGoey, L. P. H., 1995, "Modeling of Burner-Stabilized Hydrogen/Air Flames Using Mathematically Reduced Reaction Schemes," *Combustion Science and Technology*, Vol. 107, pp. 165-180.

Fedkiw, R. P., Merriman, B., and Osher, S., 1997, "High Accuracy Numerical Methods for Thermally Perfect Gas Flows with Chemistry," *Journal of Computational Physics*, Vol. 132, pp. 175-190.

Fedkiw, R. P., Marquina, A., and Merriman, B., 1999, "An Isobaric Fix for the Overheating Problem in Multimaterial Compressible Flows," *Journal of Computational Physics*, Vol. 148, pp. 545-78.

Frenklach, M., 1991, "Reduction of Chemical Reaction Models," in *Numerical Approaches to Combustion Modeling*, E. S. Oran and J. P. Boris, eds., *Progress in Aeronautics and Astronautics*, Vol. 135, pp. 129-154.

Frenklach, F., Wang, H., and Rabinowitz, M. J., 1992, "Optimization and Analysis of Large Chemical Kinetic Mechanisms Using the Solution Mapping Method–Combustion of Methane," *Progress in Energy and Combustion Science*, Vol. 18, No. 1, pp. 47-73.

Ghia, U., Ghia, K. N., and Shin, C. T., 1982, "High-Re Solutions for Incompressible-Flow Using the Navier-Stokes Equations and a Multigrid Method," *Journal of Computational Physics*, Vol. 48, No. 3, pp. 387-411.

Golub, G. H., and Van Loan, C. F., 1996, *Matrix Computations*, Baltimore, MD: Johns Hopkins.

Goussis, D. A., and Lam, S. H., 1992, "A Study of Homogeneous Methanol Oxidation Kinetics Using CSP," *Twenty-Fourth Symposium (International) on Combustion*, The Combustion Institute, pp. 113-120.

Hindmarsh, A. C., 1983, ODEPACK, A systematized collection of ODE solvers *Scientific Computing*, R. S. Stepleman *et al.*, eds., pp. 55-64.

Kee, R. J., Rupley, F. M., and Miller, J. A., 1990, The Chemkin Thermodynamic Data Base, Sandia National Laboratories Report SAND87-8215B.

Lam, S. H., 1993, "Using CSP to Understand Complex Chemical Kinetics," *Combustion Science and Technology*, Vol. 89, Nos. 5-6, pp. 375-404.

LeVeque, R. J., 1992, *Numerical Methods for Conservation Laws*, Basel: Birkhäuser.

Liandrat, J., Tchamitchian, P., 1990, "Resolution of the 1D Regularized Burgers Equation Using a Spatial Wavelet Approximation," NASA Contractor Report 187480, ICASE Report 90-83, NASA Langley Research Center, Hampton VA.

Maas, U., and Pope, S. B., 1992a, "Implementation of Simplified Chemical Kinetics Based on Intrinsic Low-Dimensional Manifolds," *Twenty-Fourth Symposium (International) on Combustion*, The Combustion Institute, pp. 103-112.

Maas, U., and Pope, S. B., 1992b, "Simplifying Chemical Kinetics: Intrinsic Low-Dimensional Manifolds in Composition Space," *Combustion and Flame*, Vol. 88, pp. 239-264.

Maas, U., and Pope, S. B., 1994, "Laminar Flame Calculations Using Simplified Chemical Kinetics Based on Intrinsic Low-Dimensional Manifolds," *Twenty-Fifth Symposium (International) on Combustion*, The Combustion Institute, pp. 1349-1356.

Maas, U., 1998, "Efficient Calculation of Intrinsic Low-Dimensional Manifolds for the Simplification of Chemical Kinetics," *Computing Visualization Science*, Vol. 1, pp. 69-81.

Maas, U., and Warnatz, J., 1988, "Ignition Processes in Hydrogen-Oxygen Mixtures," *Combustion and Flame*, Vol. 74, pp. 53-69.

Menikoff, R., 1994, "Errors When Shock-Waves Interact Due to Numerical Shock Width," *SIAM Journal of Scientific Computing*, Vol. 15, pp. 1227-42.

Meyer, Y., 1990, *Ondelettes et Opérateurs*, Hermann: Paris.

Powers, J. M., Paolucci, S., Rastigejev, Y., and Singh, S., 1999, "A Wavelet/ILDM Method for Computational Combustion," *Bulletin of the American Physical Society*, Vol. 44, No. 8, p. 54.

Radhakrishnan, K., 1991, "Combustion Kinetics and Sensitivity Analysis Computations," in *Numerical Approaches to Combustion Modeling*, E. S. Oran and J. P. Boris, eds., *Progress in Aeronautics and Astronautics*, Vol. 135, pp. 83-128.

Rastigejev, Y., and Paolucci, S., 1999, "The Use of Wavelets in Computational Fluid Mechanics," in *Proceedings of the 3rd ASME/JSME Joint Fluids Engineering Conference*, Paper FEDSM99-7162.

Rastigejev, Y., Singh, S., Bowman, C., Paolucci, S., and Powers, J. M., 2000, "Novel Modeling of Hydrogen/Oxygen Detonation," AIAA-2000-0318, 38th AIAA Aerospace Sciences Meeting and Exhibit, Reno, NV.

Rastigejev, Y., and Paolucci, S., 2002, "Wavelet Based Adaptive Multilevel Algorithm for Solving PDEs," *Journal of Scientific Computing*, to be submitted.

Saad, Y. and Schultz, M.H., 1986, "GMRES: A Generalized Minimal Residual Algorithm for Solving Nonsymmetric Linear Systems," *SIAM Journal of Scientific and Statistical Computing*, Vol. 7, pp. 856-869.

Saito, N. and Beylkin, G., 1993, "Multiresolution Representations Using the Auto-Correlation Functions of Compactly Supported Wavelets," *IEEE Transactions on Signal Processing*, Vol. 41, pp. 3584-3590.

Schmidt, D., Segatz, J., Riedel, U., Warnatz, J., and Maas, U., 1996, "Simulation of Laminar Methane-Air Flames Using Automatically Simplified Chemical Kinetics," *Combustion Science and Technology*, Vol. 113-114, pp. 3-16.

Singh, S., Powers, J. M., and Paolucci, S., 1999, "Multidimensional Detonation Solutions from Reactive Navier-Stokes Equations," Proceedings of the 17th International Colloquium on the Dynamics of Explosions and Reactive Systems, Heidelberg, Germany.

Singh, S., and Powers, J. M., 1999, "Modeling Gas Phase RDX Combustion with Intrinsic Low Dimensional Manifolds," Proceedings of the 17th International Colloquium on the Dynamics of Explosions and Reactive Systems, Heidelberg, Germany.

Singh, S., Rastigejev, Y., Paolucci, S., and Powers, J. M., 2001, "Resolved Viscous Detonation in $H_2/O_2/Ar$ Using Intrinsic Low Dimensional Manifolds and Wavelet Adaptive Multilevel Representation," *Combustion Theory and Modeling*, Vol. 5, pp. 163-184.

Smooke, M. D., 1991a, "Numerical Modeling of Laminar Diffusion Flames," in *Numerical Approaches to Combustion Modeling*, E. S. Oran and J. P. Boris, eds., *Progress in Aeronautics and Astronautics*, Vol. 135, pp. 183-223.

Smooke, M. D., 1991b, *Reduced Kinetic Mechanisms and Asymptotic Approximations for Methane-Air Flames*, Springer-Verlag: Berlin.

Strang, G., 1968, On the Construction and Comparison of Difference Schemes *SIAM Journal of Numerical Analysis* Vol. 5, pp. 506-17.

Treviño, C. and Méndez, F., 1992, "Reduced Kinetic Mechanism for Methane Ignition," *Twenty-Fourth Symposium (International) on Combustion*, The Combustion Institute, pp. 121-127.

Vasilyev, O. V. and Paolucci, S., 1996, "A Dynamically Adaptive Multilevel Wavelet Collocation Method for Solving Partial Differential Equations in a Finite Domain," *Journal of Computational Physics*, Vol. 125, pp. 498-512.

Vasilyev, O. V. and Paolucci, S., 1997, "A Fast Adaptive Wavelet-Collocation Algorithm for Multi-Dimensional PDEs," *Journal of Computational Physics*, Vol. 138, pp. 16-56.

Vasilyev, O. V., Paolucci, S., and Sen, M., 1995, "A Multilevel Wavelet Collocation Method for Solving Partial Differential Equations in a Finite Domain," *Journal of Computational Physics*, Vol. 120, pp. 33-47.

Vlachos, D. G., 1996, "Reduction of Detailed Kinetic Mechanisms for Ignition and Extinction of Premixed Hydrogen/Air Flames, *Chemical Engineering Science*, Vol. 51, No. 16, pp. 3979-3993.

Warnatz, J., 1992, "Resolution of Gas Phase and Surface Combustion Chemistry into Elementary Reactions," *Twenty-Fourth Symposium (International) on Combustion*, The Combustion Institute, pp. 553-579.

Williams, F. A., 1985, *Combustion Theory*, Benjamin Cummings: Menlo Park.